

Article

Cr-Zn/Ni-Containing Nanocomposites as Effective Magnetically Recoverable Catalysts for CO₂ Hydrogenation to Methanol: The Role of Metal Doping and Polymer Co-Support

Svetlana A. Sorokina ¹, Nina V. Kuchkina ¹ , Maxim E. Grigoriev ², Alexey V. Bykov ², Andrey K. Ratnikov ¹, Valentin Yu. Doluda ², Mikhail G. Sulman ² and Zinaida B. Shifrina ^{1,*}

¹ A.N. Nesmeyanov Institute of Organoelement Compounds, Russian Academy of Sciences, 28 Vavilov St., Moscow 119991, Russia

² Department of Biotechnology and Chemistry, Tver State Technical University, 22 A. Nikitina St., Tver 170026, Russia

* Correspondence: shifrina@ineos.ac.ru

Abstract: CO₂ hydrogenation to methanol is an important process that could solve the problem of emitted CO₂ that contributes to environmental concern. Here we developed Cr-, Cr-Zn-, and Cr-Ni-containing nanocomposites based on a solid support (SiO₂ or Al₂O₃) with embedded magnetic nanoparticles (NPs) and covered by a cross-linked pyridylphenylene polymer layer. The decomposition of Cr, Zn, and Ni precursors in the presence of supports containing magnetic oxide led to formation of amorphous metal oxides evenly distributed over the support-polymer space, together with the partial diffusion of metal species into magnetic NPs. We demonstrated the catalytic activity of Cr₂O₃ in the hydrogenation reaction of CO₂ to methanol, which was further increased by 50% and 204% by incorporation of Ni and Zn species, respectively. The fine intermixing of metal species ensures an enhanced methanol productivity. Careful adjustment of constituent elements, e.g., catalytic metal, type of support, presence of magnetic NPs, and deposition of hydrophobic polymer layer contributes to the synergetic promotional effect required for activation of CO₂ molecules as well. The results of catalytic recycle experiments revealed excellent stability of the catalysts due to protective role of hydrophobic polymer.

Keywords: methanol synthesis; CO₂ hydrogenation; magnetic nanoparticles; chromium oxide; nanocomposites; supported catalyst; polymer layer



Citation: Sorokina, S.A.; Kuchkina, N.V.; Grigoriev, M.E.; Bykov, A.V.; Ratnikov, A.K.; Doluda, V.Y.; Sulman, M.G.; Shifrina, Z.B. Cr-Zn/Ni

-Containing Nanocomposites as Effective Magnetically Recoverable Catalysts for CO₂ Hydrogenation to Methanol: The Role of Metal Doping and Polymer Co-Support. *Catalysts*

2023, 13, 1. <https://doi.org/10.3390/catal13010001>

Academic Editor: Victorio Cadierno

Received: 17 November 2022

Revised: 9 December 2022

Accepted: 15 December 2022

Published: 20 December 2022



Copyright: © 2022 by the authors. Licensee MDPI, Basel, Switzerland. This article is an open access article distributed under the terms and conditions of the Creative Commons Attribution (CC BY) license (<https://creativecommons.org/licenses/by/4.0/>).

1. Introduction

Human impact on the environment has become a critical issue for the last 20 years. Emissions of greenhouse gases are now believed to be responsible for global warming and have gained worldwide concern. CO₂ is one of the most emitted gases with level in the atmosphere raised from 315 ppm in 1958 when continuous observations began to 420 ppm in 2021 [1,2]. In this regard, CO₂ utilization and transformation into valuable chemicals are of particular importance.

CO₂ can be considered as a carbon feedstock alternative to hydrocarbons whose combustion depletes the carbon sources. The possible transformation routes for CO₂ molecule via catalytic hydrogenation include the formation of formic acid, methane, methanol, and DME [3,4]. The production of methanol from CO₂ is considered as one of the most effective ways for decreasing the CO₂ concentration [5,6]. Methanol is an important platform molecule which can be converted into a variety of reagents, such as formaldehyde, acetic acids, and others [7–9]. It is a component of fuel blends, antifreezes, resins, and plastics [10]. Currently methanol is almost exclusively synthesized from syngas via Fischer-Tropsch process over the Cu-ZnO-Al₂O₃ catalyst [11]. However, recent reports

have defined CO₂ methanolization as one of the most exciting commercial applications for CO₂ capture [4,10,12,13].

The heterogeneous catalysts employed for CO₂ to methanol hydrogenation are usually ternary catalytic systems comprised of bimetallic species deposited on a solid support. While Cu-ZnO-based materials are the most investigated systems due to high activity and ability to operate under moderate reaction conditions, recent studies have been focused on expanding the scope of catalytic systems and chemical element combinations [13,14]. Thus, Cu-In [15], Pd-Zn [16–18], Rh-In [19], Pd-Cu [20], and Ni-Ga [21,22] catalytic systems have been explored. The key role of support is also highlighted in numerous papers [14,23]. A strong metal-support interaction may direct the reaction pathway, enhancing the selectivity and activity. For example, Ni-based catalysts without proper modification deliver only methane as a main product of CO₂ hydrogenation, while Ni deposited on Ga₂O₃ provides methanol with high selectivity [22]. The effect of metal-support interaction is attributed to the electronic and structural modification due to formation of oxygen vacancies, electronic doping, formation of alloy interface, and charged metal moieties, etc. [14,24–26]. Al₂O₃, CeO₂, ZrO₂, SiO₂, and TiO₂ are the widely examined solid materials for this purpose.

However, the explored catalysts usually suffer from relatively poor activity and low selectivity due to the presence of reverse water-gas shift (RWGS) reaction that proceeds along with the target hydrogenation reaction. RWGS reaction leads to the formation of CO and H₂O vapors lowering the methanol yield [14]. Moreover, water vapors also cause a notable decrease in catalyst stability and reusability [27,28]. Another major shortcoming of the nanosized catalysts used in methanol synthesis is the NP agglomeration that occurs due to the sintering process induced by high-reaction temperature and pressure [29,30]. Strong and reliable stabilization of NPs may suppress the sintering. This could be achieved by appropriate interactions with a support and/or incorporation of additional ligand molecules creating a barrier between metal species [23].

Therefore, novel catalysts developed for methanol synthesis from CO₂ should withstand harsh reaction conditions, preserve stability under high water partial pressure, possess high thermostability, and have easily adoptable microstructures. The synthetic procedures employed in catalyst production should be simple and scalable due to potential industrial implementation of the process.

In our preceding work, we developed the catalysts based on metal NPs stabilized by aromatic polymers for different hydrogenation reactions, such as synthesis of methanol from syngas [31–33], synthesis of gamma-valerolactone from levulinic acid [34], and furfuryl alcohol from furfural [35]. These catalysts demonstrated exceptional activity and stability which have been preserved in several consecutive catalytic cycles. The synthesis of these nanocomposites has been carried out by thermal decomposition of metal precursors in the presence of a polymer acting as a stabilizing media. Despite the precious control over the NP size and morphology provided by this technique, its employment in CO₂ methanolization is not fully reasonable because of low catalyst yield. Indeed, the approaches to nanocomposite formation providing several grams of catalyst during simple synthetic procedures are preferable. This could be achieved by addition of a solid support to the catalyst formulation. More recently, we developed an approach to the formation of a thin polymer layer on a mesoporous silica gel containing magnetic nanoparticles [36]. After incorporation of palladium species by coordination with pyridine groups of the polymer, the resulting nanocomposites were tested in Suzuki-Miyaura reaction. The results of recycle experiments revealed the important role of the branched polymer layer in NPs stabilization and superior catalytic activity under repeated use [36].

In this work, we applied this approach to fabricate the novel nanostructured catalytic systems for methanol synthesis from CO₂ + H₂. Deposition of a thin polymer layer which is hydrophobic in nature on a solid support (SiO₂ or Al₂O₃) containing metal NPs could be one of the possible strategies for attenuating the negative influence of H₂O vapors. Moreover, the polymer adsorption contributes to NP segregation and stabilization, thus

preventing the possible sintering and leaching of NPs. Both processes are known to be responsible for significant drops in the catalyst activity [29,30].

Here we synthesized and explored Cr-, Cr-Zn-, and Cr-Ni-containing magnetically recoverable catalysts based on two different inorganic supports—SiO₂ and Al₂O₃—covered by a polymer layer. Recently, Cr₂O₃ has been shown to possess a potential activity in CO₂ methanolization [37] while having an established productivity in the methanol synthesis from syngas [33,38,39]. The oxygen vacancies presented on the surface of Cr₂O₃ make it suitable for activation of thermodynamically stable and inert CO₂ molecule [37,40]. The activity of Cr₂O₃ can be adopted by doping with different metals like Ni, La, etc. [41]. In this work we expanded the studies of Cr₂O₃ catalytic activity in methanol synthesis via CO₂ hydrogenation. To elucidate the main factors underlying the high-catalyst activity, we fabricated both monometallic and bimetallic catalytic systems. Magnetic NPs included in the catalyst structure do not possess the catalytic activity in this reaction; however, they may boost methanol productivity while ensuring the effective magnetic separation for repeated uses and more sustainable processes.

2. Results and Discussion

To meet requirements for effective CO₂ methanolization the designed catalytic system should be (1) stable under harsh reaction conditions and high partial pressure of water vapors, (2) easily separable from reaction mixture to allow the repeated uses, and (3) synthesized via robust procedure. To develop such catalyst, we used a combination of synthetic methods.

At the first step, Fe₃O₄ NPs were formed in the pores of commercially available mesoporous solid support according to the procedure described previously [42]. Here we used two different supports: Al₂O₃ and SiO₂ to further assess their influence on the catalytic activity. Thermal decomposition of iron nitrate in the presence of the support and mild reducing agent led to the formation of magnetic nanoparticles of 13.2 and 15.6 nm for SiO₂- and Al₂O₃-based composites, respectively, oriented alongside the pores [42,43]. Magnetic NPs ensure the easy and simple separation of catalyst from the reaction mixture by external magnet. After formation of magnetic support, a thin layer of cross-linked pyridylphenylene polymer (PPP) has been deposited by Diels Alder polycondensation of two branched monomers in the presence of magnetic silica/alumina. Structure of PPP together with the scheme of formation of a solid support -Fe₃O₄ -PPP composite are given in Figure S1 in SI. PPP is a thermally stable polymer whose thermal decomposition starts at 500 °C which is important for practical application [32,34]. It is worth noting that deposition of PPP on the surface of support does not decrease the porosity of material due to cross-linked hyperbranched structure, as was established earlier [36]. This means that a polymer layer does not hinder the active sites of the future catalyst and does not prevent the diffusion of substrate molecules. The presence of pyridine moieties in PPP structure may contribute to more effective chemisorption of CO₂ molecules being the first step of catalysis because of electropositivity of CO₂ carbon atom.

The metal species, namely Cr, Cr-Zn, and Cr-Ni, have been incorporated into the structure of SiO₂/Al₂O₃-Fe₃O₄-PPP composites by wet impregnation method of corresponding metal acetyl acetonates followed by a thermal decomposition in a furnace tube at 350 °C. To elucidate the possible promoting effect of Fe₃O₄ molecules, the nanocomposites without magnetic NPs have been synthesized as well.

2.1. Structure and Morphology of the Nanocomposites

To identify the position of all species in the composites, STEM EDS mapping was performed. Figure 1 shows the STEM dark field image and EDS maps of SiO₂-Fe₃O₄-PPP-Cr-Zn nanocomposite. The carbon map demonstrates a full coverage of silica by polymer layer. Fe map totally repeats the shape of Si map indicating the formation of Fe₃O₄ NPs in silica pores. Cr and Zn maps are similar to Fe map which may correspond to the incorporation of Cr and Zn species in magnetite structure. It is worth noting that

deposition of catalytic species on the top of magnetic oxide with formation of heterogeneous hybrid nanocomposite is more preferable for effective catalysis rather than homogeneous nucleation of separately being Cr_2O_3 and ZnO_2 nanoparticles [25,44].

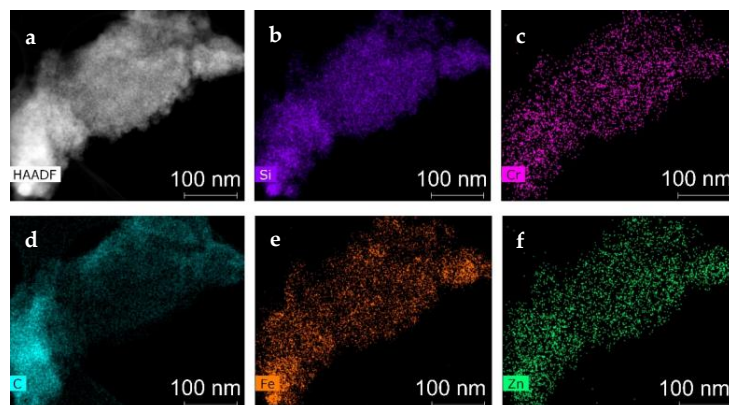


Figure 1. STEM dark field image (a) and EDS maps of Si (b), Cr (c), C (d), Fe (e) and Zn (f) of $\text{SiO}_2\text{-Fe}_3\text{O}_4\text{-PPP-Cr-Zn}$ nanocomposite.

STEM EDS images for $\text{SiO}_2\text{-Fe}_3\text{O}_4\text{-PPP-Cr-Ni}$ nanocomposite are given in Figure 2. Again, C, Si, Fe, Cr, and Ni maps show a good fit revealing the formation of magnetic and catalytic species in the silica covered by polymer. However, Ni species are distributed across the sample with some aggregation of NPs. This may be due to a poor intermixing of Ni species with a magnetite phase.

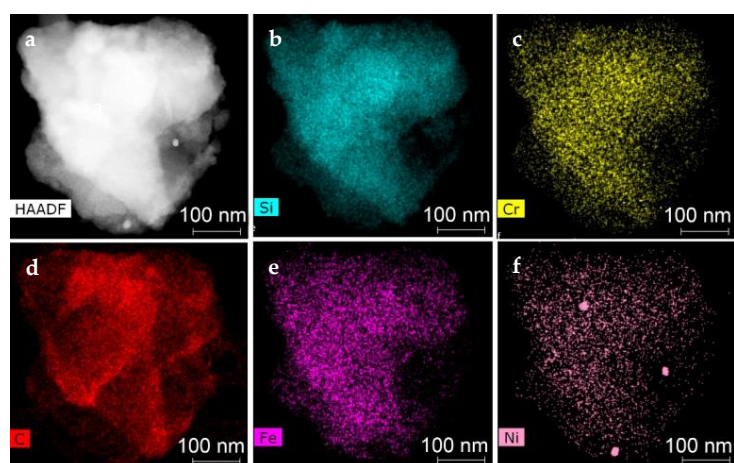


Figure 2. STEM dark field image (a) and EDS maps of Si (b), Cr (c), C (d), Fe (e) and Ni (f) of $\text{SiO}_2\text{-Fe}_3\text{O}_4\text{-PPP-Cr-Ni}$ nanocomposite.

STEM EDS maps of $\text{Al}_2\text{O}_3\text{-Fe}_3\text{O}_4\text{-PPP-Cr-Zn}$, $\text{SiO}_2\text{-PPP-Cr-Zn}$, and $\text{SiO}_2\text{-Fe}_3\text{O}_4\text{-PPP-Cr}$ are presented in Figures S2–S4, respectively. Replacement of SiO_2 with Al_2O_3 did not influence the deposition of PPP on the support. The positions of metal species for all composites demonstrated their perfect distribution over the support-polymer area and a good correlation with Fe map.

To assess the chemical composition of the materials obtained, EDS spectra were recorded (Figure 3a,b for $\text{SiO}_2\text{-Fe}_3\text{O}_4\text{-PPP-Cr-Zn}$, and $\text{SiO}_2\text{-Fe}_3\text{O}_4\text{-PPP-Cr-Ni}$, respectively, and Figure S5a,b for $\text{SiO}_2\text{-PPP-Cr-Zn}$ and $\text{SiO}_2\text{-Fe}_3\text{O}_4\text{-PPP-Cr}$, respectively). The spectra confirmed the presence of constituent elements together with successful deposition of a polymer layer which is evidenced by the presence of carbon in the composite. The elemental compositions for all samples are given in Table S1.

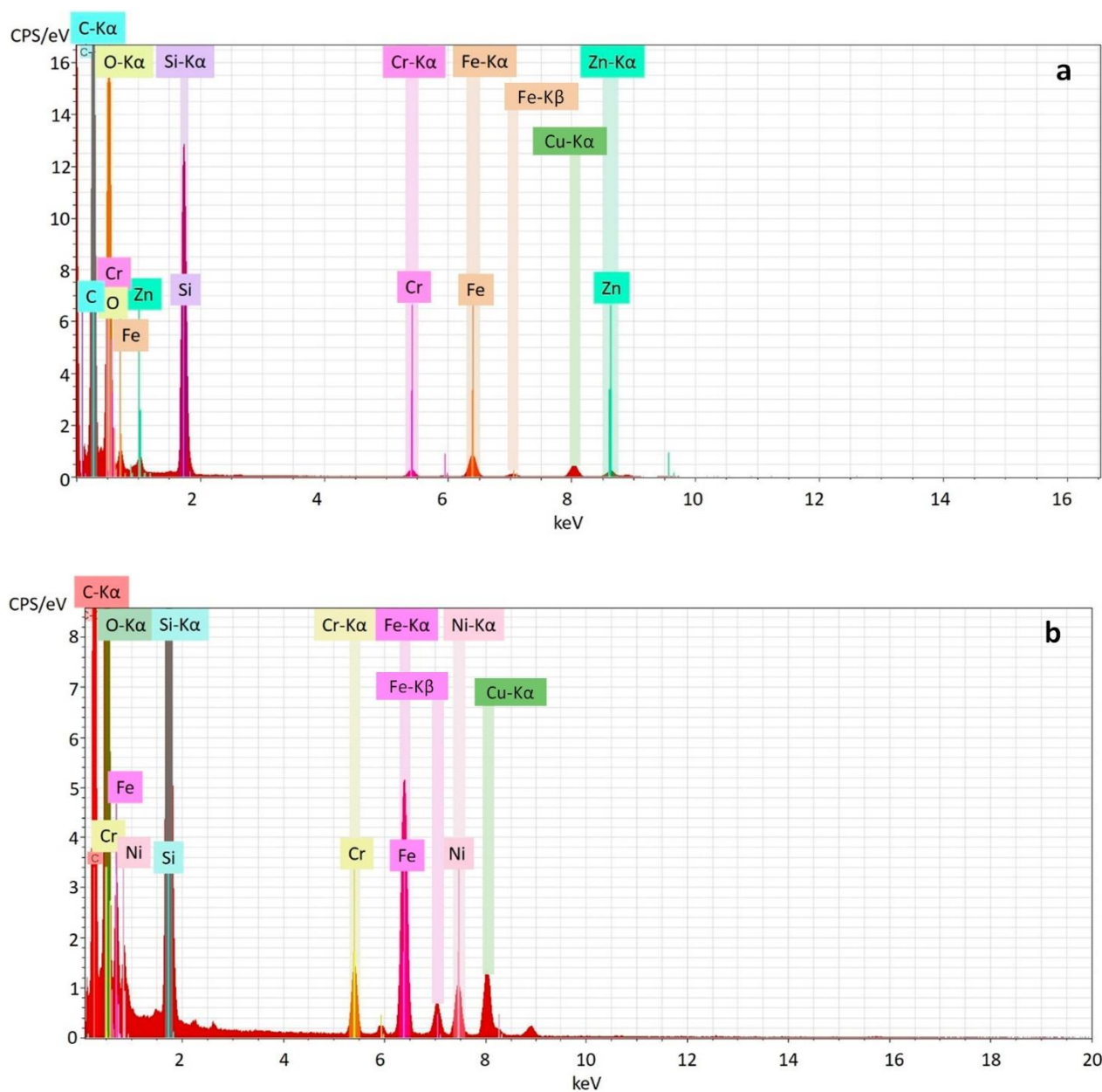


Figure 3. EDS spectra of $\text{SiO}_2\text{-Fe}_3\text{O}_4\text{-PPP-Cr-Zn}$ (a) and $\text{SiO}_2\text{-Fe}_3\text{O}_4\text{-PPP-Cr-Ni}$ (b) nanocomposites. Cu-K α signals are presented due to Cu-grid used for recording of the spectra.

Figure 4 displays the XRD spectra of $\text{SiO}_2\text{-Fe}_3\text{O}_4\text{-PPP}$ (a), $\text{SiO}_2\text{-Fe}_3\text{O}_4\text{-PPP-Cr-Zn}$ (b), and $\text{SiO}_2\text{-Fe}_3\text{O}_4\text{-PPP-Cr-Ni}$ (c) nanocomposites, which are very similar to each other and show a polymer halo at $\sim 10^\circ 2\theta$ and a broad signal at 22° corresponding to amorphous silica. A set of reflections characteristic for a spinel structure of magnetite is also observed for all samples. Surprisingly, no additional reflections are detected, which could be attributed to the formation of zinc or chromium oxides. This could be due to the formation of amorphous oxide structures or different ferrites whose reflections are overlapped with those of Fe_3O_4 or due to intermixing of Zn, Cr, and Ni species with a magnetite phase that do not disturb the Fe_3O_4 crystalline structure. The more careful inspection of XRD-spectra revealed a slight shift of (311) peak of Fe_3O_4 to smaller angles for Cr-Zn-containing composites. The enlarged depiction of this region is presented in Figure S6. This could indicate a partial penetration of Cr and Zn species in a magnetite structure as it was reported earlier [42,45,46]. The lattice constants calculated from XRD data showed an increase from 8.3801 for $\text{SiO}_2\text{-Fe}_3\text{O}_4\text{-PPP}$

to 8.3982 for $\text{SiO}_2\text{-Fe}_3\text{O}_4\text{-PPP-Cr-Zn}$. The effect could be attributed to the substitution of some Fe ions with Zn^{2+} and Cr^{3+} , and formation of ferrites. Another possible explanation is the penetration of Zn^{2+} and Cr^{3+} possessing the higher ionic radii into Fe_3O_4 NP.

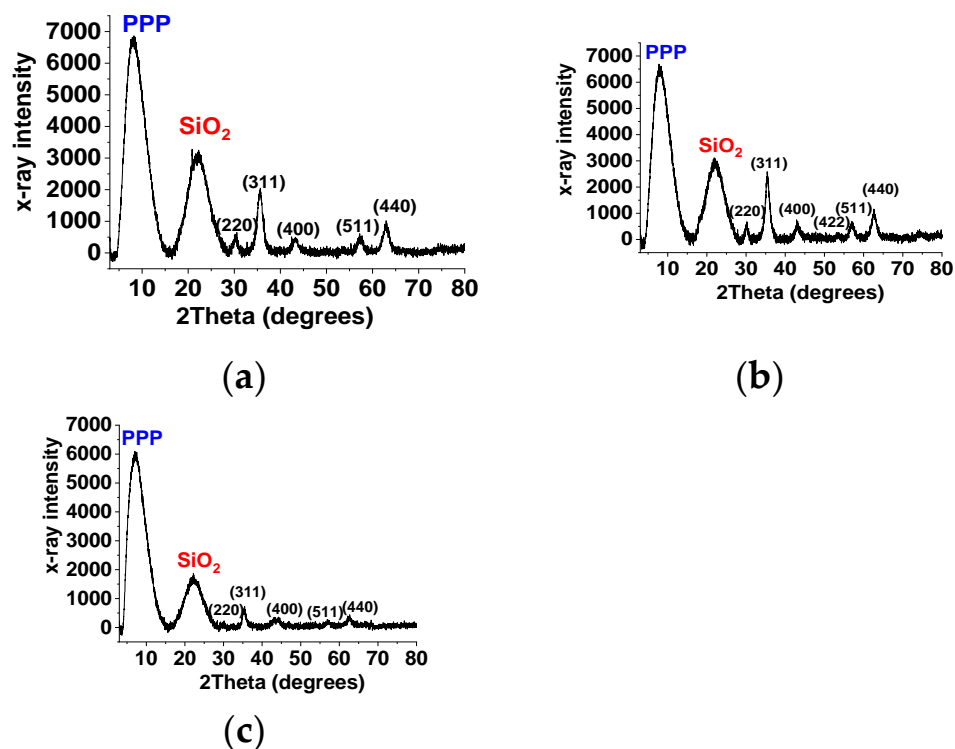


Figure 4. XRD patterns of $\text{SiO}_2\text{-Fe}_3\text{O}_4\text{-PPP}$ (a); $\text{SiO}_2\text{-Fe}_3\text{O}_4\text{-PPP-Cr-Zn}$ (b); $\text{SiO}_2\text{-Fe}_3\text{O}_4\text{-PPP-Cr-Ni}$ (c).

In case of composite without Fe_3O_4 only the signals corresponding to PPP and SiO_2 are presented in diffractogram (Figure S7a). This suggests the formation of amorphous Cr- and Zn-containing species. At the same time, for Al_2O_3 -based composites containing Fe_3O_4 , the diffraction pattern contains a set of peaks corresponding to Al_2O_3 and reflections attributed to Fe_3O_4 structure (Figure S7b,c). Similar to composites based on SiO_2 -, the reflections characteristic for Cr and Zn oxides are absent.

To achieve further insight into the structure of the composites obtained, XPS spectra were recorded. The survey spectra of the samples are given in Figure S8. The oxidation states of the metal species were analyzed by high resolution (HR) XPS. In all samples, Fe 2p spectrum contains a main peak at 711.0 eV which is typical for iron oxides [47] (Figure 5a for $\text{SiO}_2\text{-Fe}_3\text{O}_4\text{-PPP-Cr-Zn}$, and SI for other Fe_3O_4 -containing composites). A region between Fe $2p_{3/2}$ and Fe $2p_{1/2}$ displays a plateau indicating the formation of Fe_3O_4 . In the opposite case (formation of Fe_2O_3), the prevalence of Fe^{3+} ions would result in a satellite peak with binding energy 8 eV higher than the main peak [47]. Importantly, impregnation by Cr, Zn, and Ni species do not disturb the $\text{Fe}^{3+}/\text{Fe}^{2+}$ ratio. If any substitution of Fe^{2+} by Zn^{2+} or Ni^{2+} would appear, which took place upon the formation of ferrites structures like ZnFe_2O_4 , NiFe_2O_4 , ZnCrFeO_4 , or chromite, this would influence the $\text{Fe}^{3+}/\text{Fe}^{2+}$ ratio and lead to the occurrence of additional signals, in particular the satellite peak, or peak shifting (See Figures) [48,49]. However, the Fe 2p spectra before and after incorporation of metal compounds are similar (See Figure 5a and Figure S9).

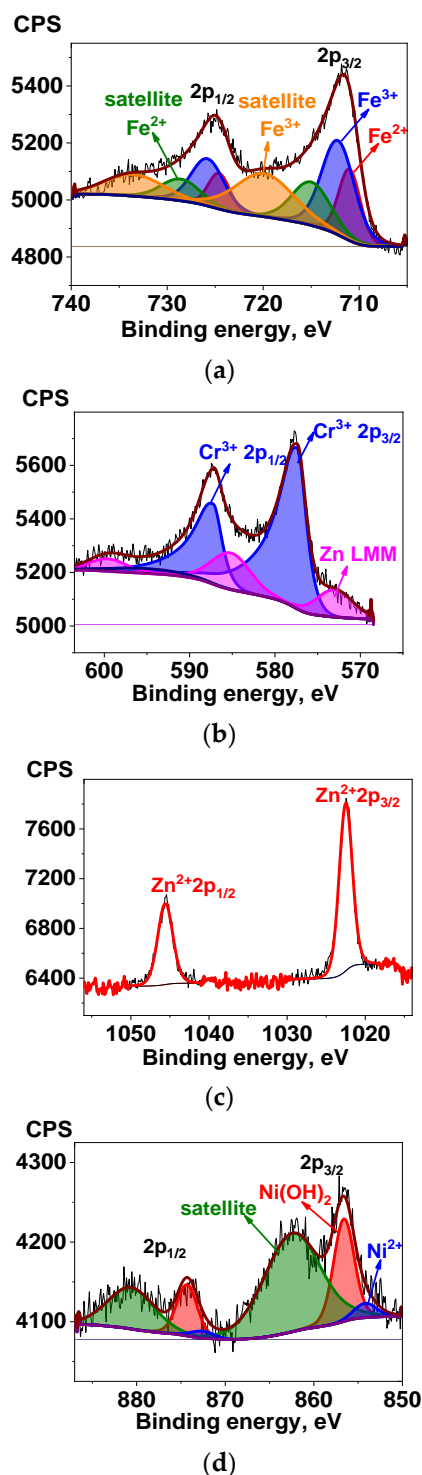


Figure 5. HR XPS spectra of SiO₂-Fe₃O₄-PPP-Cr-Zn in the Fe 2p (a); Cr 2p (b); Zn 2p (c) regions; and Ni 2p (d) of SiO₂-Fe₃O₄-PPP-Cr-Ni.

The analysis of Cr 2p XPS spectra (Figure 5b) revealed that Cr solely exists in the form of Cr³⁺. The spin-orbit splitting energy (Cr 2p_{3/2}–Cr 2p_{1/2} = 9.76 eV) coincides with that of Cr₂O₃ [50]. The positions of peaks at Zn 2p XPS spectra with binding energies of 1022.8 and 1045.9 eV for 2p_{3/2} and 2p_{1/2}, respectively, correspond to Zn²⁺ typical for ZnO (Figure 5c) [51]. For Ni-containing composite, the positions of peaks at HR XPS spectrum match Ni²⁺ state in oxide-hydroxide form [49,52,53] (Figure 5d). The deconvolution parameters for all spectra are summarized in Tables S2–S7. HR XPS of Fe, Cr, and Zn for all

nanocomposites are presented in SI, Figures S9–S13. The positions of the main peaks are consistent with those described in Figure 5.

Thus, one can conclude that formation of ferrites is not observed, and decomposition of Cr, Zn, and Ni precursors leads to formation of amorphous metal oxides. However, considering the peak shifting (Figure S6) and increase in the values of lattice constants revealed by XRD, we assumed the possible diffusion of Cr, Zn, and Ni species into magnetic NPs. This assumption is based on XPS data for 2p and 3p electrons. 2p electrons are known to possess considerably lower kinetic energy than that of 3p electrons. Thus, the contribution of 2p electrons in the spectrum reflects the surface concentration of the element, while 3p electrons characterize the deeper layers of the material. Data on 2p and 3p content of the metals in the nanocomposites are presented in Table 1. As one can see, the enrichment of the surface with metal is dependent on the metal type. For all samples, the composites surface was enriched with Cr^{3+} species since the chrome content for 2p electrons was higher than that of 3p electrons. However, small amount of Cr^{3+} species were able to penetrate the deeper magnetite NP level as well. For Ni-containing samples, XPS data show the surface accumulation of Ni species. Surprisingly, Zn content was higher for 3p electrons which means a higher fraction of Zn in the deeper layers rather than at the surface. This phenomenon could be explained by a better compatibility of Zn^{2+} with Fe_3O_4 in comparison with that of Cr^{3+} and Ni^{2+} . Although, the possibility of solid solution and alloy formation is governed by Hume-Rothery rules, small metal clusters do not always follow the rules [54]. In addition, the thermal decomposition of zinc acetyl acetonate starts at 190 °C and ZnO NPs formation was reported to proceed at 195 °C [55,56]. For chromium acetyl acetonate, the decomposition temperature is much higher (250 °C) [57]. The differences in decomposition temperature and consequent earlier destruction of Zn precursor are another reason for deeper migration of Zn^{2+} into a magnetite structure in comparison with Cr^{3+} .

Table 1. Atomic concentrations of metals for Cr-, Zn-, and Ni-containing magnetic nanocomposites determined by HR XPS for 2p and 3p transitions.

Sample	Relative Content by XPS, Atomic %			
	Fe 2p/3p	Cr 2p/3p	Zn 2p/3p	Ni 2p/3p
$\text{SiO}_2\text{-Fe}_3\text{O}_4\text{-PPP-Cr-Zn}$	0.50/0.30	0.41/0.07	0.23/0.32	-
$\text{SiO}_2\text{-Fe}_3\text{O}_4\text{-PPP-Cr-Ni}$	0.55/0.26	0.54/0.09	-	0.45/0
$\text{Al}_2\text{O}_3\text{-Fe}_3\text{O}_4\text{-PPP-Cr-Zn}$	0.52/0.31	0.41/0.08	0.25/0.31	-

To conclude, most probably the decomposition of Cr, Zn, and Ni acetyl acetonates, in the presence of magnetite-containing solid supports covered by PPP, results in the formation of thin metal oxide layers on $\text{SiO}_2(\text{Al}_2\text{O}_3)\text{-Fe}_3\text{O}_4\text{-PPP}$ composites together with a partial diffusion of metal oxides into magnetic NP. The diffusion was the most prominent for Zn^{2+} ions and slightly occurred for Cr^{3+} . Such intermixing does not influence the $\text{Fe}^{3+}/\text{Fe}^{2+}$ ratio and the magnetite structure was preserved in all samples. Considering the structural data obtained, the formation of ferrite structures like ZnFe_2O_4 , ZnCrFeO_4 , and NiFe_2O_4 were not established. Therefore, intermixing of ZnO and Cr_2O_3 with magnetite NP stands at the intermediate stage before the ferrite formation which has been reported elsewhere [48].

Since the adsorption of CO_2 and H_2 plays an important role for the CO_2 hydrogenation process, the adsorption capacities of the composites have been estimated by CO_2 and H_2 temperature-programmed desorption (TPD) measurements. The results are presented in Figures 6 and 7. To elucidate the polymer ability to enhance the CO_2 adsorption, measurements were carried out for parent $\text{SiO}_2\text{-Fe}_3\text{O}_4$ and after deposition of PPP- $\text{SiO}_2\text{-Fe}_3\text{O}_4\text{-PPP}$ (Figure 6a). Placement of a thin polymer layer on a solid support significantly increases the CO_2 adsorption. While parent $\text{SiO}_2\text{-Fe}_3\text{O}_4$ is characterized by two types of adsorption centers (moderate center at 266 °C and strong center at 478 °C) with the total amount of adsorbed CO_2 equal to 0.015 mmol/g, the addition of PPP results in noticeable

changes in adsorption centers. The appearance of new desorption peaks at 244 °C, 294 °C, 366 °C, and 562 °C is accompanied by increase in CO₂ amount up to 0.035 mmol/g. The effect is undoubtedly attributed to the presence of basic pyridine centers in PPP structure. Since the CO₂ adsorption is the first step of the catalytic reaction, introduction of PPP into the catalyst structure should enhance the catalysis rate due to advanced CO₂ adsorption.

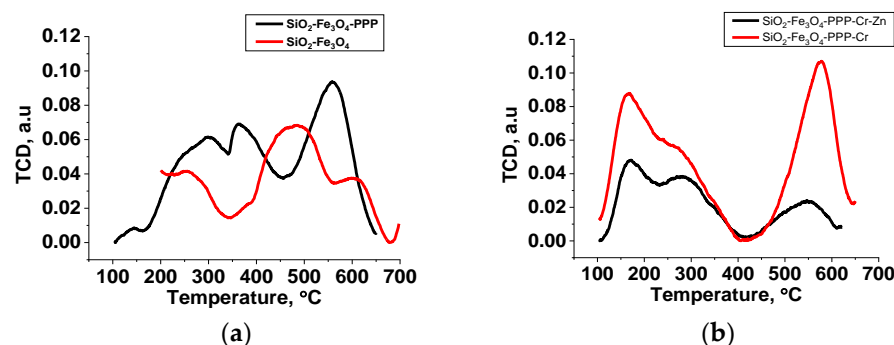


Figure 6. CO₂-TPD results of the examined catalysts: (a) SiO₂-Fe₃O₄ (red line) and SiO₂-Fe₃O₄-PPP (black line); and (b): SiO₂-Fe₃O₄-PPP-Cr (red line) and SiO₂-Fe₃O₄-PPP-Cr-Zn (black line).

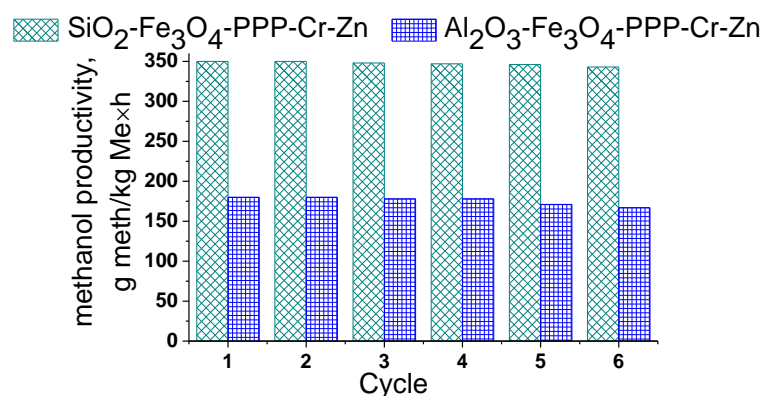


Figure 7. Recycling experiments for SiO₂-Fe₃O₄-PPP-Cr-Zn (green column) and Al₂O₃-Fe₃O₄-PPP-Cr-Zn (blue column) in CO₂ hydrogenation. Reaction conditions are: 250 °C, 5 MPa, 50 mg of the catalyst, CO₂:H₂ = 1:4, 15 mL of dodecane, 6 h.

The incorporation of metal species further influenced the CO₂ adsorption capacities of the composites (Figure 6b). Thus, monometallic SiO₂-Fe₃O₄-PPP-Cr showed the adsorption capacity of 0.073 mmol/g exceeding that of SiO₂-Fe₃O₄-PPP. It is worth noting that strong adsorption centers (at 562 °C) arising due to PPP structure are retained in composites with catalytically active metals. Formation of bimetallic composites leads to weakening of total basicity to 0.032 mmol/g. Nevertheless, the composites efficiently adsorb CO₂ which is a prerequisite for effective catalysis.

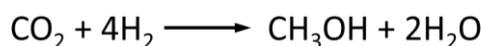
The H₂ adsorption capacities of the synthesized nanocomposites were also estimated (Figure S14a,b). Similarly, deposition of PPP leads to an increase in amount of adsorbed H₂ (0.023 mmol/g for SiO₂-Fe₃O₄ vs 0.03 mmol/g for SiO₂-Fe₃O₄-PPP). Incorporation of metal species and formation of bimetallic nanocomposite increases the total amount of adsorbed H₂ to 0.043 mmol/g.

2.2. Catalytic Properties of Nanocomposites in CO₂ Hydrogenation

Cr-, Cr-Zn-, and Cr-Ni-containing nanocomposites have been tested in CO₂ hydrogenation to methanol. The process is challenging due to the high thermodynamic stability of CO₂ molecule. The formation of methanol from CO₂ is energetically undesired, implying the high temperature and pressure along with structural promotion of the catalyst should

be applied to obtain the sufficient methanol productivity. Table 2 displays the results of the catalyst performance. The widely accepted approach to assess the catalyst activity in this reaction is to calculate the methanol productivity rate per the catalyst amount and per the metal content. The activity of the catalysts was compared with commercial catalyst MegaMax 800. To elucidate the optimal ratio of the metals, nanocomposites with different metal loadings have also been synthesized. Here we focused on the best catalytic results obtained, while the activity of the composites differed in metal ratio is given in SI, Table S8.

Table 2. Catalytic properties of the nanocomposites in methanol synthesis from CO₂ + H₂.



Sample Notation	Content by Elemental Analysis, wt%				Conversion, %	Selectivity, %	Methanol Productivity, g Methanol/kg Me ×.h
	Fe	Cr	Zn	Ni			
SiO ₂ -Fe ₃ O ₄ -PPP	9.1	-	-	-	-	-	×.h
SiO ₂ -Fe ₃ O ₄ -PPP-Cr	6.8	2.1	-	-	4.2	98.3	115
SiO ₂ -Fe ₃ O ₄ -PPP-Cr-Ni	4.3	2.2	-	2.3	6.0	98.5	172
SiO ₂ -Fe ₃ O ₄ -PPP-Cr-Zn	4.1	2.0	2.1	-	9.4	99.1	350
Al ₂ O ₃ -Fe ₃ O ₄ -PPP-Cr-Zn	4.3	2.2	2.1	-	6.2	98.6	195
SiO ₂ -PPP-Cr-Zn	-	2.1	2.0	-	4.1	99.0	120
MegaMax 800					4.8	87.5	78

Reaction conditions: 250 °C, 5 MPa, CO₂:H₂ = 1:4, 15 mL of dodecane, 50 mg of the catalyst, 6 h.

The magnetic silica with deposited PPP expectedly shows no catalytic activity. The monometallic composite SiO₂-Fe₃O₄-PPP-Cr provides the methanol productivity comparable with that of a commercial catalyst. The result confirms the ability of Cr₂O₃ to catalyze the methanol synthesis from CO₂ and H₂. The incorporation of additional metals leads to an increase in the catalyst activity with the highest methanol productivity observed for the Cr-Zn-containing composite. Notably, the SiO₂-based, Cr-Zn-containing composite was in two orders of magnitude more active than Al₂O₃-based system prepared with the same metal loadings. The catalytic activity of the composite without magnetic NPs-SiO₂-PPP-Cr-Zn-was considerably lower than that of the Fe₃O₄-containing sample, revealing the promoting effect provided by Fe₃O₄ NPs. It also should be noted that a decrease in metal loading leads to a decrease in catalytic activity (Table S8).

To analyze the enhanced catalytic activity of SiO₂-based systems, the nitrogen adsorption-desorption measurements were carried out. The adsorption isotherms are presented in Figure S15. The analysis revealed the distinct textural properties of SiO₂ vs Al₂O₃ composites with the smaller BET surface area and pore sizes of the latter. This could have a detrimental effect on the catalyst activity due to worse accessibility of active catalytic species and diffusion limitations. Several studies also report a positive influence of SiO₂ on catalytic activity in CO₂ hydrogenation reaction. The addition of SiO₂ as itself to convenient Cu-ZnO-Al₂O₃ catalyst increased the activity and enhanced CuO dispersion [58]. The similar promoting effect has been observed in another study [59]. SiO₂-modified Cu-ZnO-ZrO₂ catalyst exhibits a better catalytic activity and higher long-term stability in comparison with a non-modified system due to a better intermixing of metal oxide components [59]. SiO₂ has also been shown to accelerate the selective hydrogenation of CO₂ to methanol for Co-based catalysts [60]. The effect was attributed to efficient stabilization of methoxy *CH₃O species being intermediates in the catalytic process by interface formed between SiO₂ and catalytic metal—Me-O-SiO_n. Our results support the data on the promotional effect of silica on methanol synthesis from CO₂, and highlight the importance of careful adjustment and optimization of catalyst composition by the appropriate choice of support.

Our results demonstrated that the introduction of magnetic NPs in catalyst structure along with convenience and simplicity of magnetic separation provided the promoting effect on methanol productivity. We assume that Fe₃O₄ NPs serve as a reservoir for a better intermixing and dispersion of ZnO and Cr₂O₃ components. Such assumption is supported by XPS data. This led to a closer contact between catalytic species being a

prerequisite for effective catalytic performance. The positive effect of spinel structures of Fe_3O_4 on methanol synthesis has also been reported previously [42,61]. The addition of Fe_3O_4 to Cu-Zn-based catalyst results in improved methanol selectivity and enhanced catalyst activity. Magnetic NPs have also been shown to induce a strong metal support interaction (SMSI) effect due to formation of oxygen vacancies that stabilize the reaction intermediates and activate CO_2 molecule [42,62,63].

To conclude, each structural element in the designed nanocomposites influences the catalytic activity and the synergistic effect between catalyst constituents such as: support, polymer layer, magnetic NPs, and metal species ensures high catalytic activity and stability. The type of support determines distribution of metal species, accessibility of active centers, and occurrence of strong metal-support interactions which were shown to positively influence the catalysis. Here we demonstrated the advantages of SiO_2 support over Al_2O_3 . Magnetic NPs boost the catalyst activity due to metal intermixing and migration of catalytic species onto Fe_3O_4 surface, as was observed by XPS data on 2p/3p electron content and XRD analysis. The precious miscibility of metal species allows for better catalytic performance, as was evidenced by the higher activity of Cr-Zn-containing catalyst over Cr-Ni-one. Bimetallic Cr-containing systems were shown to outperform monometallic ones. The results are consistent with the data on the activity of other heterogeneous catalysts for CO_2 hydrogenation, and bimetallic systems typically demonstrate a better catalytic performance [4,10,13,14]. The formation of bimetallic interfaces notably lowers the activation barrier of CO_2 to methanol hydrogenation compared to monometallic systems [64]. For industrial Cu-ZnO- Al_2O_3 catalyst, Cu-ZnO interface is believed to be the active site [65]. Moreover, the formation of bimetallic interfaces is usually followed by the formation of oxygen vacancies which are crucial for CO_2 activation and intermediate stabilization [14,63]. In particular, chromium doping with metals has been shown to induce the oxygen vacancy formation [41,66].

Comparison of the catalytic results with the literature data undoubtedly demonstrated the advantages of the proposed approach to creation of effective catalysts for the synthesis of methanol from CO_2 [67–75]. The results of recycling experiments revealed the exceptional stability of the catalysts after six repetitive uses. The methanol productivity rate was preserved at nearly 98% for SiO_2 -based catalysts, while 5% drop of activity was observed for Al_2O_3 -containing systems starting from the fifth use (Figure 7). We believe that superior catalyst stability is due to the protective role of the hydrophobic polymer layer. In contrast to the PPP-covered $\text{SiO}_2/\text{Al}_2\text{O}_3$ -catalysts, the conventional catalytic systems show 11% drop of activity after 36 h of catalytic experiment [30]. The deactivation was induced by agglomeration of ZnO species and sintering of Cu particles for CuO-ZnO- Al_2O_3 system [30]. Sintering and NP aggregation have also been proved to be the main reason of deactivation for other catalytic systems [29].

To elucidate the polymer layer role, the catalysts after catalysis have been separated from the reaction mixture with external magnet and analyzed by STEM EDS. $\text{SiO}_2\text{-Fe}_3\text{O}_4\text{-PPP-Cr-Zn}$ and $\text{Al}_2\text{O}_3\text{-Fe}_3\text{O}_4\text{-PPP-Cr-Zn}$ have been chosen for analysis. The results are presented in Figures S16 and S17. For both samples, Cr- and Zn-species remained evenly distributed over all samples with no visible bulk NPs which could be due to the aggregation of metal species during catalysis. The results confirm the outstanding stability of the catalytic systems. Therefore, the deposition of PPP not only facilitates the catalytic reaction through the enhanced adsorption of CO_2 , but also ensures the structural separation of NPs against sintering.

3. Materials and Methods

3.1. Materials

Iron (III) nitrate nonahydrate (ABCR, 98%), mesoporous silica gels (Sigma-Aldrich, Darmstadt, Germany, 6 nm, 200–425 mesh), aluminum oxide (Sigma-Aldrich, 5.8 nm, 150 mesh), zinc acetylacetonate hydrate (Sigma-Aldrich), chromium (III) acetylacetonate (Sigma-Aldrich, 97%), nickel (II) acetylacetonate (ABCR, 98%), ethylene glycol (Sigma-

Aldrich, 99%), and diphenyl ether (Sigma-Aldrich, 99%) were used as received. Acetone (99.5%) and ethanol (96%) were purchased from “Component-reactive” and used as received. Magnetic NPs in the pores of mesoporous silica gel and aluminum oxide were synthesized according to procedures published in [42,43], respectively. Deposition of polymer PPP layer on the surface of magnetic silica gel was performed as described previously [36]. Monomers for the synthesis of PPP in the presence of solid support (see Figure S1) were synthesized according to [76].

3.2. Synthesis of Al_2O_3 - Fe_3O_4 -PPP

Al_2O_3 - Fe_3O_4 (0.2027 g) was heated in a Schlenk reaction flask under flowing argon atmosphere at 120 °C for 2 h to remove moisture. Monomer A6 (50 mg, 0.037 mmol) was dissolved in 3 mL of dichloromethane. This solution was added to Al_2O_3 - Fe_3O_4 and sonicated for 20 min to allow the monomer to adsorb on the Al_2O_3 - Fe_3O_4 surface. The flask was placed in a rotary evaporator and the solvent was evacuated. B2 (0.087 g, 0.111 mmol) was dissolved in 3 mL of diphenyl ether and added to the reaction flask containing A6 deposited on Al_2O_3 - Fe_3O_4 . The reaction flask was filled with argon and heated at 160 °C for 10 h upon stirring. The final material (Al_2O_3 - Fe_3O_4 -PPP) was collected from the suspension using a rare earth magnet, washed with dichloromethane (8×10 mL), and dried at room temperature overnight in vacuo. The elemental analysis data: N 1.23%, C 25.45%, H 1.89%.

3.3. Synthesis of Catalytically Active Nanocomposites

In a typical experiment, 0.23 g of zinc acetylacetonate were dissolved in 10 mL of acetone, followed by a dropwise addition to 2.57 g of Fe_3O_4 - SiO_2 -PPP (or Al_2O_3 - Fe_3O_4 -PPP). After acetone evaporation, the solution containing 0.70 g of chromium (III) acetylacetonate dissolved in 10 mL of acetone was added to Fe_3O_4 - SiO_2 -PPP (or Al_2O_3 - Fe_3O_4 -PPP) coated with zinc acetylacetonate. The mixture was allowed to stir for 3 h in air for acetone evaporation. The sample was then dried in a vacuum oven at room temperature for 12 h. Then the sample was heated in a tube furnace under argon with 7% of H_2 to 350 °C with a heating rate of 2 °C/min. The temperature was held at 350 °C for 3 h and then the sample was cooled to room temperature. For the Cr-Ni-containing sample (SiO_2 - Fe_3O_4 -PPP-Cr-Ni), 0.22 g of nickel acetyl acetonate was added instead of zinc precursor. For SiO_2 - Fe_3O_4 -PPP-Cr nanocomposite, only 0.70 g of chromium (III) acetylacetonate in 10 mL of acetone was used. To assess the metal content in the resulted nanocomposites, X-ray fluorescence (XRF) measurements were applied.

3.4. Characterization

Transmission electron microscopy (TEM), scanning transmission electron microscopy (STEM), and energy-dispersive X-ray (EDX) microanalysis was carried out in an Osiris TEM/STEM (Thermo Fisher Scientific, Waltham, MA, USA) equipped with a high angle annular dark field detector (HAADF) (Fischione, Export, PA, USA) and an X-ray energy dispersive spectrometer Super X (ChemiSTEM, Bruker, Bradford County, FL, USA) at an accelerating voltage of 200 kV. Specimens for TEM, STEM, and EDXS studies were prepared by placement of the Lacey carbon film on Cu grid into the vial with the suspension of the nanocomposite in CH_2Cl_2 .

Powder X-ray diffraction patterns were recorded using Proto AXRD Θ -2 Θ diffractometer (Detroit, MI, USA) with copper anode ($K\alpha = 1.541874 \text{ \AA}$, Ni- $K\beta$ filter) and 1D-detector Dectris Mythen 1K in the angular range $2\theta = 5$ – 100° . A scanning step was set to be 0.02° and the speed was $0.5^\circ/\text{min}$. Identification was performed with the PDXL software (Rigaku Corporation, Tokyo, Japan) using the ICDD PDF-2 database (2017).

X-ray photoelectron spectroscopy (XPS) data were obtained using Axis Ultra DLD (Kratos) spectrometer (Kyoto, Japan) with a monochromatic Al $K\alpha$ radiation. All the data were acquired at X-ray power of 150 W. Survey spectra were recorded at an energy step of 1 eV with an analyzer pass energy 160 eV, and high-resolution spectra were recorded at an

energy step of 0.1 eV with an analyzer pass energy 40 eV. Samples were out-gassed for 180 min before analysis. The data analysis was performed by CasaXPS.

Carbon dioxide temperature programmed desorption experiments were made using AutoChem HP chemisorption analyzer (Norcross, GA, USA). For carbon dioxide desorption experiments synthesized samples were placed in quartz cuvette and placed in analyzer module. The sample was heated in helium atmosphere up to 700 °C, then cooled down to 105 °C, and flashed with carbon dioxide for one hour followed by flashing with pure helium for one hour. Afterwards, the sample was heated to 700 °C with a temperature gradient of 10 °C/min and carbon dioxide desorption curve was recorded. Quantity of basic sites were calculated according to quantity of chemisorbed carbon dioxide using preliminary made calibration curve.

Hydrogen temperature programmed desorption experiments were made using AutoChem HP chemisorption analyzer. For hydrogen desorption experiments synthesized samples were placed in quartz cuvette and placed in analyzer module. The sample was heated in argon atmosphere up to 700 °C, then cooled down to ambient temperature, and flashed with mixture of 10 v.% of hydrogen in argon for one hour followed by flashing with pure argon for one hour. Afterwards, the sample was heated to 700 °C with a temperature gradient of 10 °C/min and hydrogen desorption curves were recorded. Quantity of hydrogen-capable adsorption sites were calculated according to quantity of chemisorbed hydrogen using preliminary made calibration curve.

Zn, Cr, and Ni content of the composites was obtained from X-ray fluorescence (XRF) measurements using a Zeiss Jena VRA-30 spectrometer (Oberkochen, Germany) equipped with a Mo anode, a LiF200 crystal analyzer, and a SD detector.

3.5. Catalytic Study

In a typical experiment, 50 mg of the catalyst and 15 mL of dodecane were loaded in the stainless-steel reactor (7) (internal volume of 50 mL) equipped with a propeller mixer (stirring rate 250 rpm). Then the hydrogen pressure was set to 5.0 MPa, the reactor was purged with hydrogen for 3 times, and the mixture was heated up to 250 °C. When the above temperature was achieved, the catalyst was reduced for 1 h, then the hydrogen was substituted for the gas mixture ($H_2/CO_2 = 4/1$) and stirring rate was increased up to 750 rpm. Reaction was provided for six hours followed by cooling to ambient temperature. Gas phase was directed into the chromatographic system of on-line analysis along the heated line through the return pressure valve and removed from the system through a flowmeter. Liquid phase was analyzed using GS-MS Shimadzu 2010 (Kyotocity, Japan) gas chromatomass spectrometer using preliminary made calibration curves. Methanol accumulation rate was calculated taking into account mass of formed methanol in reaction media, catalysts mass and reaction time.

For repeated catalytic experiments, the catalyst after reaction was collected with an external magnet in a vial, washed thoroughly with ethanol, and dried in vacuo until the constant weight. The reaction conditions for recycling experiments were similar to those described above.

4. Conclusions

In this work, novel $SiO_2/Al_2O_3-Fe_3O_4-PPP-Cr-Me$ ($Me = Zn, Ni$) catalysts possessing high activity and exceptional stability in CO_2 hydrogenation reaction to methanol have been synthesized. The developed approach to synthesis of the catalysts offers several possibilities for structural adoption that boost the catalytic activity due to the synergetic effect Synthesized $SiO_2/Al_2O_3-Fe_3O_4-PPP$ composites providing a carrier for deposition and dispersion of catalytically active metal species as well as a structural barrier against sintering. Presence of a hydrophobic heteroaromatic polymer layer on the silica and alumina supports prevents the aggregation of catalytically active species, elevates the stability of the catalyst, and facilitates CO_2 hydrogenation through enhanced adsorption of CO_2 and H_2 . Magnetic NPs facilitate the reaction rate through the structural promotion,

probably due to formation of oxygen vacancies, and allow for fast and simple magnetic separation of the catalyst for repeated uses as well. Creation of bimetallic interface by combination of two metals (Cr-Zn and Cr-Ni) enhances the catalytic activity with the highest methanol productivity achieved for the Cr-Zn-containing composite. Considering the robust synthetic procedures, high activity attained for non-noble metals, easy catalyst recovery, and excellent stability over six consecutive catalytic cycles, the proposed approach can be considered as a promising strategy for improving the performance of the catalysts in production of methanol from $\text{CO}_2 + \text{H}_2$.

Supplementary Materials: The following supporting information can be downloaded at: <https://www.mdpi.com/article/10.3390/catal13010001/s1>, Figure S1: Schematic presentation of deposition of a thin layer of pyridylphenylene polymer on a solid support; Figure S2: STEM EDS maps of $\text{Al}_2\text{O}_3\text{-Fe}_3\text{O}_4\text{-PPP-Cr-Zn}$; Figure S3: STEM EDS maps of $\text{SiO}_2\text{-PPP-Cr-Zn}$. Figure S4: STEM EDS maps of $\text{SiO}_2\text{-Fe}_3\text{O}_4\text{-PPP-Cr}$. Figure S5: EDS spectra of $\text{SiO}_2\text{-PPP-Cr-Zn}$ (a) and $\text{SiO}_2\text{-Fe}_3\text{O}_4\text{-PPP-Cr}$ (b) nanocomposites; Figure S6: XRD patterns of the samples in the area of the (311) spinel peak; Figure S7: XRD patterns of $\text{SiO}_2\text{-PPP-Cr-Zn}$ (a), $\text{Al}_2\text{O}_3\text{-Fe}_3\text{O}_4\text{-PPP}$ (b), $\text{Al}_2\text{O}_3\text{-Fe}_3\text{O}_4\text{-PPP-Cr-Zn}$ (c); Figure S8: XPS survey spectra of the $\text{SiO}_2\text{-Fe}_3\text{O}_4\text{-PPP-Cr-Zn}$ (a), $\text{SiO}_2\text{-Fe}_3\text{O}_4\text{-PPP-Cr}$ (b), $\text{SiO}_2\text{-PPP-Cr-Zn}$ (c), $\text{SiO}_2\text{-Fe}_3\text{O}_4\text{-PPP-Cr-Ni}$ (d), $\text{Al}_2\text{O}_3\text{-Fe}_3\text{O}_4\text{-PPP-Cr-Zn}$ (e) nanocomposites; Figure S9: HR XPS of Fe 2p of $\text{SiO}_2\text{-Fe}_3\text{O}_4\text{-PPP}$ before incorporation of metal oxides in the nanocomposite structure; Figure S10: HR XPS of Fe 2p (a) and Cr 2p (b) regions of $\text{SiO}_2\text{-Fe}_3\text{O}_4\text{-PPP-Cr}$; Figure S11: HR XPS of Cr 2p (a) and Zn 2p (b) regions of $\text{SiO}_2\text{-PPP-Cr-Zn}$; Figure S12: HR XPS of Fe 2p (a), Cr 2p (b) and Ni 2p (c) regions of $\text{SiO}_2\text{-Fe}_3\text{O}_4\text{-PPP-Cr-Ni}$; Figure S13: HR XPS of Fe 2p (a), Cr 2p (b) and Zn 2p (c) regions of $\text{Al}_2\text{O}_3\text{-Fe}_3\text{O}_4\text{-PPP-Cr-Zn}$; Figure S14. H_2 -TPD results of the examined catalysts: (a) $\text{SiO}_2\text{-Fe}_3\text{O}_4$ (red line) and $\text{SiO}_2\text{-Fe}_3\text{O}_4\text{-PPP}$ (black line) and (b): $\text{SiO}_2\text{-Fe}_3\text{O}_4\text{-PPP-Cr}$ (red line) and $\text{SiO}_2\text{-Fe}_3\text{O}_4\text{-PPP-Cr-Zn}$ (black line). Figure S15: N_2 adsorption-desorption isotherms (a,c) and pore sizes distributions (b,d) of $\text{Al}_2\text{O}_3\text{-Fe}_3\text{O}_4\text{-PPP}$ (a,c) and $\text{SiO}_2\text{-Fe}_3\text{O}_4\text{-PPP}$ (c,d). $S_{\text{BET}} = 164 \text{ m}^2/\text{g}$ ($\text{Al}_2\text{O}_3\text{-Fe}_3\text{O}_4\text{-PPP}$) and $S_{\text{BET}} = 246 \text{ m}^2/\text{g}$ ($\text{SiO}_2\text{-Fe}_3\text{O}_4\text{-PPP}$); Figure S16: STEM dark field image (a) EDS maps of Si (b), Cr (c), C (d), Fe (e) and Zn (f) of $\text{SiO}_2\text{-Fe}_3\text{O}_4\text{-PPP-Cr-Zn}$ nanocomposite after catalysis; Figure S17: STEM dark field image (a) EDS maps of Al (b), Zn (c), C (d), Fe (e) and Cr (f) of $\text{Al}_2\text{O}_3\text{-Fe}_3\text{O}_4\text{-PPP-Cr-Zn}$ nanocomposite after catalysis. Table S1: Atomic percentage of elements in samples; Table S2: Fitting parameters for HR XPS of Fe 2p, Cr 2p and Zn 2p of $\text{SiO}_2\text{-Fe}_3\text{O}_4\text{-PPP-Cr-Zn}$; Table S3: Fitting parameters for HR XPS of Fe 2p of $\text{SiO}_2\text{-Fe}_3\text{O}_4\text{-PPP}$; Table S4: Fitting parameters for HR XPS of Fe 2p and Cr 2p of $\text{SiO}_2\text{-Fe}_3\text{O}_4\text{-PPP-Cr}$; Table S5: Fitting parameters for HR XPS Cr 2p and Zn 2p of $\text{SiO}_2\text{-PPP-Cr-Zn}$; Table S6: Fitting parameters for HR XPS of Fe 2p, Cr 2p and Ni 2p of $\text{SiO}_2\text{-Fe}_3\text{O}_4\text{-PPP-Cr-Ni}$; Table S7: Fitting parameters for HR XPS of Fe 2p, Cr 2p and Zn 2p of $\text{Al}_2\text{O}_3\text{-Fe}_3\text{O}_4\text{-PPP-Cr-Zn}$. Table S8. Catalytic properties of the nanocomposites in methanol synthesis from $\text{CO}_2 + \text{H}_2$.

Author Contributions: S.A.S., methodology, writing—original draft preparation, N.V.K., methodology, visualization, M.E.G., investigation, A.V.B., resources, A.K.R., visualization, investigation, V.Y.D., investigation, M.G.S., conceptualization, Z.B.S., conceptualization, writing—review and editing, supervision, data curation, project administration. All authors have read and agreed to the published version of the manuscript.

Funding: This research was funded by Russian Science Foundation, grant number 22-43-02025.

Data Availability Statement: Not applicable.

Acknowledgments: The assistance of A.L. Vasiliev, Federal Scientific Research Centre, Shubnikov Institute of Crystallography, in recording of STEM EDS images is gratefully acknowledged. The contribution of the Centre for Molecular Composition Studies of the INEOS RAS (elemental analysis) with financial support from Ministry of Science and Higher Education of the Russian Federation is gratefully acknowledged.

Conflicts of Interest: The authors declare no conflict of interest.

References

1. Dudley, B. *BP Statistical Review of World Energy*; BP Statistical Review: London, UK, 2019.
2. Friedlingstein, P.; Jones, M.W.; O'Sullivan, M.; Andrew, R.M.; Bakker, D.C.E.; Hauck, J.; Le Quéré, C.; Peters, G.P.; Peters, W.; Pongratz, J.; et al. Global Carbon Budget 2021. *Earth Syst. Sci. Data* **2022**, *14*, 1917–2005. [[CrossRef](#)]
3. Aresta, M.; Dibenedetto, A.; Angelini, A. Catalysis for the Valorization of Exhaust Carbon: From CO₂ to Chemicals, Materials, and Fuels. Technological Use of CO₂. *Chem. Rev.* **2014**, *114*, 1709–1742. [[CrossRef](#)] [[PubMed](#)]
4. Ye, R.-P.; Ding, J.; Gong, W.; Argyle, M.D.; Zhong, Q.; Wang, Y.; Russell, C.K.; Xu, Z.; Russell, A.G.; Li, Q.; et al. CO₂ hydrogenation to high-value products via heterogeneous catalysis. *Nat. Commun.* **2019**, *10*, 5698. [[CrossRef](#)]
5. Sempuga, B.C.; Yao, Y. CO₂ hydrogenation from a process synthesis perspective: Setting up process targets. *J. CO₂ Util.* **2017**, *20*, 34–42. [[CrossRef](#)]
6. Saeidi, S.; Amin, N.A.S.; Rahimpour, M.R. Hydrogenation of CO₂ to value-added products—A review and potential future developments. *J. CO₂ Util.* **2014**, *5*, 66–81. [[CrossRef](#)]
7. Ni, Y.; Shi, L.; Liu, H.; Zhang, W.; Liu, Y.; Zhu, W.; Liu, Z. A green route for methanol carbonylation. *Catal. Sci. Technol.* **2017**, *7*, 4818–4822. [[CrossRef](#)]
8. Wingad, R.L.; Bergström, E.J.E.; Everett, M.; Pellow, K.J.; Wass, D.F. Catalytic conversion of methanol/ethanol to isobutanol—a highly selective route to an advanced biofuel. *Chem. Commun.* **2016**, *52*, 5202–5204. [[CrossRef](#)]
9. Li, T.; Shoinkhorova, T.; Gascon, J.; Ruiz-Martínez, J. Aromatics Production via Methanol-Mediated Transformation Routes. *ACS Catal.* **2021**, *11*, 7780–7819. [[CrossRef](#)]
10. Zhang, X.; Zhang, G.; Song, C.; Guo, X. Catalytic Conversion of Carbon Dioxide to Methanol: Current Status and Future Perspective. *Front. Energy Res.* **2021**, *8*, 621119. [[CrossRef](#)]
11. Behrens, M.; Studt, F.; Kasatkin, I.; Köhl, S.; Hävecker, M.; Abild-Pedersen, F.; Zander, S.; Girgsdies, F.; Kurr, P.; Kniep, B.-L.; et al. The Active Site of Methanol Synthesis over Cu/ZnO/Al₂O₃ Industrial Catalysts. *Science* **2012**, *336*, 893–897. [[CrossRef](#)]
12. Olah, G.A. Beyond Oil and Gas: The Methanol Economy. *Angew. Chem. Int. Ed.* **2005**, *44*, 2636–2639. [[CrossRef](#)]
13. Álvarez, A.; Bansode, A.; Urakawa, A.; Bavykina, A.V.; Wezendonk, T.A.; Makkee, M.; Gascon, J.; Kapteijn, F. Challenges in the Greener Production of Formates/Formic Acid, Methanol, and DME by Heterogeneously Catalyzed CO₂ Hydrogenation Processes. *Chem. Rev.* **2017**, *117*, 9804–9838. [[CrossRef](#)] [[PubMed](#)]
14. Ren, M.; Zhang, Y.; Wang, X.; Qiu, H. Catalytic Hydrogenation of CO₂ to Methanol: A Review. *Catalysts* **2022**, *12*, 403. [[CrossRef](#)]
15. Shi, Z.; Tan, Q.; Tian, C.; Pan, Y.; Sun, X.; Zhang, J.; Wu, D. CO₂ hydrogenation to methanol over Cu-In intermetallic catalysts: Effect of reduction temperature. *J. Catal.* **2019**, *379*, 78–89. [[CrossRef](#)]
16. Bahruji, H.; Bowker, M.; Hutchings, G.; Dimitratos, N.; Wells, P.; Gibson, E.; Jones, W.; Brookes, C.; Morgan, D.; Lalev, G. Pd/ZnO catalysts for direct CO₂ hydrogenation to methanol. *J. Catal.* **2016**, *343*, 133–146. [[CrossRef](#)]
17. Diez, J.; Valverde, J.; Sánchez, P.; Dorado, F. CO₂ Hydrogenation to Methanol at Atmospheric Pressure: Influence of the Preparation Method of Pd/ZnO Catalysts. *Catal. Lett.* **2016**, *146*, 373–382. [[CrossRef](#)]
18. Xu, J.; Su, X.; Liu, X.; Pan, X.; Pei, G.; Huang, Y.; Wang, X.; Zhang, T.; Geng, H. Methanol synthesis from CO₂ and H₂ over Pd/ZnO/Al₂O₃: Catalyst structure dependence of methanol selectivity. *Appl. Catal. A Gen.* **2016**, *514*, 51–59. [[CrossRef](#)]
19. Wang, J.; Sun, K.; Jia, X.; Liu, C.-j. CO₂ hydrogenation to methanol over Rh/In₂O₃ catalyst. *Catal. Today* **2021**, *365*, 341–347. [[CrossRef](#)]
20. Jiang, X.; Koizumi, N.; Guo, X.; Song, C. Bimetallic Pd–Cu catalysts for selective CO₂ hydrogenation to methanol. *Appl. Catal. B Environ.* **2015**, *170–171*, 173–185. [[CrossRef](#)]
21. Gallo, A.; Snider, J.L.; Sokaras, D.; Nordlund, D.; Kroll, T.; Ogasawara, H.; Kovarik, L.; Duyar, M.S.; Jaramillo, T.F. Ni₅Ga₃ catalysts for CO₂ reduction to methanol: Exploring the role of Ga surface oxidation/reduction on catalytic activity. *Appl. Catal. B Environ.* **2020**, *267*, 118369. [[CrossRef](#)]
22. Studt, F.; Sharafutdinov, I.; Abild-Pedersen, F.; Elkjær, C.F.; Hummelshøj, J.S.; Dahl, S.; Chorkendorff, I.; Nørskov, J.K. Discovery of a Ni–Ga catalyst for carbon dioxide reduction to methanol. *Nat. Chem.* **2014**, *6*, 320–324. [[CrossRef](#)] [[PubMed](#)]
23. Kattel, S.; Liu, P.; Chen, J.G. Tuning Selectivity of CO₂ Hydrogenation Reactions at the Metal/Oxide Interface. *J. Am. Chem. Soc.* **2017**, *139*, 9739–9754. [[CrossRef](#)] [[PubMed](#)]
24. Elnabawy, A.O.; Schimmenti, R.; Cao, A.; Nørskov, J.K. Why ZnO is the Support for Cu in Methanol Synthesis? A Systematic Study of the Strong Metal Support Interactions. *ACS Sustain. Chem. Eng.* **2022**, *10*, 1722–1730. [[CrossRef](#)]
25. Kuld, S.; Thorhauge, M.; Falsig, H.; Elkjær, C.F.; Helveg, S.; Chorkendorff, I.; Sehested, J. Quantifying the promotion of Cu catalysts by ZnO for methanol synthesis. *Science* **2016**, *352*, 969–974. [[CrossRef](#)]

26. Stangeland, K; Li, H; Yu, Z. CO₂ hydrogenation to methanol: The structure–activity relationships of different catalyst systems. *Energy Ecol. Environ.* **2020**, *5*, 272–285. [[CrossRef](#)]
27. Behrens, M. Promoting the Synthesis of Methanol: Understanding the Requirements for an Industrial Catalyst for the Conversion of CO₂. *Angew. Chem. Int. Ed.* **2016**, *55*, 14906–14908. [[CrossRef](#)]
28. Gao, P; Zhong, L; Zhang, L; Wang, H; Zhao, N; Wei, W; Sun, Y. Yttrium oxide modified Cu/ZnO/Al₂O₃ catalysts via hydrotalcite-like precursors for CO₂ hydrogenation to methanol. *Catal. Sci. Technol.* **2015**, *5*, 4365–4377. [[CrossRef](#)]
29. Frei, M.S; Mondelli, C; García-Muelas, R; Kley, K.S; Puértolas, B; López, N; Safonova, O.V; Stewart, J.A; Curulla Ferré, D; Pérez-Ramírez, J. Atomic-scale engineering of indium oxide promotion by palladium for methanol production via CO₂ hydrogenation. *Nat. Commun.* **2019**, *10*, 3377. [[CrossRef](#)]
30. Liang, B; Ma, J; Su, X; Yang, C; Duan, H; Zhou, H; Deng, S; Li, L; Huang, Y. Investigation on Deactivation of Cu/ZnO/Al₂O₃ Catalyst for CO₂ Hydrogenation to Methanol. *Ind. Eng. Chem. Res.* **2019**, *58*, 9030–9037. [[CrossRef](#)]
31. Baird, N; Losovyj, Y; Yuzik-Klimova, E.Y; Kuchkina, N.V; Shifrina, Z.B; Pink, M; Stein, B.D; Morgan, D.G; Wang, T; Rubin, M.A; et al. Zinc-Containing Magnetic Oxides Stabilized by a Polymer: One Phase or Two? *ACS Appl. Mater. Interfaces* **2016**, *8*, 891–899. [[CrossRef](#)]
32. Baird, N; Dittmar, J.W; Losovyj, Y.B; Morgan, D.G; Stein, B.D; Pink, M; Kuchkina, N.V; Serkova, E.S; Lependina, O.L; Grigoriev, M.E; et al. Enhancing the Catalytic Activity of Zn-Containing Magnetic Oxides in a Methanol Synthesis: Identifying the Key Factors. *ACS Appl. Mater. Interfaces* **2017**, *9*, 2285–2294. [[CrossRef](#)]
33. Baird, N; Dittmar, J.W; Losovyj, Y.B; Pink, M; Morgan, D.G; Stein, B.D; Torozova, A.S; Krasnova, I.Y; Grigoriev, M.E; Sidorov, A.I; et al. Cr-Containing Magnetic Oxides in a Methanol Synthesis: Does Cr Ion Distribution Matter? *Chem. Sel.* **2017**, *2*, 6269–6276. [[CrossRef](#)]
34. Sorokina, S.A; Mikhailov, S.P; Kuchkina, N.V; Bykov, A.V; Vasiliev, A.L; Ezernitskaya, M.G; Golovin, A.L; Nikoshvili, L.Z; Sulman, M.G; Shifrina, Z.B. Ru@hyperbranched Polymer for Hydrogenation of Levulinic Acid to Gamma-Valerolactone: The Role of the Catalyst Support. *Int. J. Mol. Sci.* **2022**, *23*, 799. [[CrossRef](#)] [[PubMed](#)]
35. Alibegovic, K; Morgan, D.G; Losovyj, Y; Pink, M; Stein, B.D; Kuchkina, N.V; Serkova, E.S; Salnikova, K.E; Shifrina, Z.B; Matveeva, V.G; et al. Efficient Furfuryl Alcohol Synthesis from Furfural over Magnetically Recoverable Catalysts: Does the Catalyst Stabilizing Medium Matter? *Chem. Sel.* **2017**, *2*, 5485–5491. [[CrossRef](#)]
36. Kuchkina, N.V; Haskell, A.K; Sorokina, S.A; Torozova, A.S; Nikoshvili, L.Z; Sulman, E.M; Stein, B.D; Morgan, D.G; Bronstein, L.M; Shifrina, Z.B. Pd Catalyst Based on Hyperbranched Polypyridylphenylene Formed In Situ on Magnetic Silica Allows for Excellent Performance in Suzuki–Miyaura Reaction. *ACS Appl. Mater. Interfaces* **2020**, *12*, 22170–22178. [[CrossRef](#)]
37. Wang, Y; Tan, L; Tan, M; Zhang, P; Fang, Y; Yoneyama, Y; Yang, G; Tsubaki, N. Rationally Designing Bifunctional Catalysts as an Efficient Strategy To Boost CO₂ Hydrogenation Producing Value-Added Aromatics. *ACS Catal.* **2019**, *9*, 895–901. [[CrossRef](#)]
38. Bradford, M; Konduru, M; Fuentes, D. Characterization and application of Cr₂O₃-ZnO catalysts for methanol synthesis. *Fuel Process. Technol.* **2003**, *83*, 11–25. [[CrossRef](#)]
39. Wen-De, H; Jun, K; Yang-Dong, W; Chuan-Ming, W; Wei-Min, Y. Insights into Syngas to Methanol Conversion on Cr₂O₃ Oxide from First-Principles-based Microkinetic Simulations. *Chin. J. Chem. Phys.* **2022**, *35*, 655–663. [[CrossRef](#)]
40. Wang, Y; Gao, W; Wang, K; Gao, X; Zhang, B; Zhao, H; Ma, Q; Zhang, P; Yang, G; Wu, M; et al. Boosting the synthesis of value-added aromatics directly from syngas via a Cr₂O₃ and Ga doped zeolite capsule catalyst. *Chem. Sci.* **2021**, *12*, 7786–7792. [[CrossRef](#)]
41. Carey, J.J; Legesse, M; Nolan, M. Low Valence Cation Doping of Bulk Cr₂O₃: Charge Compensation and Oxygen Vacancy Formation. *J. Phys. Chem. C* **2016**, *120*, 19160–19174. [[CrossRef](#)]
42. Oracko, T; Jaquish, R; Losovyj, Y.B; Morgan, D.G; Pink, M; Stein, B.D; Doluda, V.Y; Tkachenko, O.P; Shifrina, Z.B; Grigoriev, M.E; et al. Metal-Ion Distribution and Oxygen Vacancies That Determine the Activity of Magnetically Recoverable Catalysts in Methanol Synthesis. *ACS Appl. Mater. Interfaces* **2017**, *9*, 34005–34014. [[CrossRef](#)] [[PubMed](#)]
43. Jaquish, R; Reilly, A.K; Lawson, B.P; Golikova, E; Sulman, A.M; Stein, B.D; Lakina, N.V; Tkachenko, O.P; Sulman, E.M; Matveeva, V.G; et al. Immobilized glucose oxidase on magnetic silica and alumina: Beyond magnetic separation. *Int. J. Biol. Macromol.* **2018**, *120*, 896–905. [[CrossRef](#)] [[PubMed](#)]
44. Saedy, S; Newton, M.A; Zabilskiy, M; Lee, J.H; Krumeich, F; Ranocchiari, M; van Bokhoven, J.A. Copper–zinc oxide interface as a methanol-selective structure in Cu–ZnO catalyst during catalytic hydrogenation of carbon dioxide to methanol. *Catal. Sci. Technol.* **2022**, *12*, 2703–2716. [[CrossRef](#)]
45. Nguyen, X.S; Zhang, G; Yang, X. Mesocrystalline Zn-Doped Fe₃O₄ Hollow Submicrospheres: Formation Mechanism and Enhanced Photo-Fenton Catalytic Performance. *ACS Appl. Mater. Interfaces* **2017**, *9*, 8900–8909. [[CrossRef](#)] [[PubMed](#)]
46. Raju, G; Murali, N; Prasad, M.S.N.A; Suresh, B; Apparao Babu, D; Gnana Kiran, M; Ramakrishna, A; Tulu Wegayehu, M; Kishore Babu, B. Effect of chromium substitution on the structural and magnetic properties of cobalt ferrite. *Mater. Sci. Energy Technol.* **2019**, *2*, 78–82. [[CrossRef](#)]
47. Yamashita, T; Hayes, P. Analysis of XPS spectra of Fe²⁺ and Fe³⁺ ions in oxide materials. *Appl. Surf. Sci.* **2008**, *254*, 2441–2449. [[CrossRef](#)]
48. Bera, S; Prince, A.A.M; Velmurugan, S; Raghavan, P.S; Gopalan, R; Panneerselvam, G; Narasimhan, S.V. Formation of zinc ferrite by solid-state reaction and its characterization by XRD and XPS. *J. Mater. Sci.* **2001**, *36*, 5379–5384. [[CrossRef](#)]

49. Biesinger, M.C.; Payne, B.P.; Grosvenor, A.P.; Lau, L.W.M.; Gerson, A.R.; Smart, R.S.C. Resolving surface chemical states in XPS analysis of first row transition metals, oxides and hydroxides: Cr, Mn, Fe, Co and Ni. *Appl. Surf. Sci.* **2011**, *257*, 2717–2730. [[CrossRef](#)]
50. Biesinger, M.C.; Brown, C.; Mycroft, J.R.; Davidson, R.D.; McIntyre, N.S. X-ray photoelectron spectroscopy studies of chromium compounds. *Surf. Interface Anal.* **2004**, *36*, 1550–1563. [[CrossRef](#)]
51. Pauly, N.; Yubero, F.; Espinós, J.P.; Tougaard, S. XPS primary excitation spectra of Zn 2p, Fe 2p, and Ce 3d from ZnO, α -Fe₂O₃, and CeO₂. *Surf. Interface Anal.* **2019**, *51*, 353–360. [[CrossRef](#)]
52. Biesinger, M.C.; Payne, B.P.; Lau, L.W.M.; Gerson, A.; Smart, R.S.C. X-ray photoelectron spectroscopic chemical state quantification of mixed nickel metal, oxide and hydroxide systems. *Surf. Interface Anal.* **2009**, *41*, 324–332. [[CrossRef](#)]
53. Peck, M.A.; Langell, M.A. Comparison of Nanoscaled and Bulk NiO Structural and Environmental Characteristics by XRD, XAFS, and XPS. *Chem. Mater.* **2012**, *24*, 4483–4490. [[CrossRef](#)]
54. Choudhury, S.; Aguiar, J.A.; Fluss, M.J.; Hsiung, L.L.; Misra, A.; Uberuaga, B.P. Non-uniform Solute Segregation at Semi-Coherent Metal/Oxide Interfaces. *Sci. Rep.* **2015**, *5*, 13086. [[CrossRef](#)] [[PubMed](#)]
55. Rudolph, G.; Henry, M.C. The Thermal Decomposition of Zinc Acetylacetonate Hydrate. *Inorg. Chem.* **1964**, *3*, 1317–1318. [[CrossRef](#)]
56. Musić, S.; Šarić, A.; Popović, S. Formation of nanosize ZnO particles by thermal decomposition of zinc acetylacetonate monohydrate. *Ceram. Int.* **2010**, *36*, 1117–1123. [[CrossRef](#)]
57. Siddiqi, M.A.; Siddiqui, R.A.; Atakan, B. Thermal stability, sublimation pressures and diffusion coefficients of some metal acetylacetonates. *Surf. Coat. Technol.* **2007**, *201*, 9055–9059. [[CrossRef](#)]
58. Zhang, L.; Zhang, Y.; Chen, S. Effect of promoter SiO₂, TiO₂ or SiO₂-TiO₂ on the performance of CuO-ZnO-Al₂O₃ catalyst for methanol synthesis from CO₂ hydrogenation. *Appl. Catal. A Gen.* **2012**, *415–416*, 118–123. [[CrossRef](#)]
59. Phongamwong, T.; Chantaprasertporn, U.; Witoon, T.; Numpilai, T.; Poo-arporn, Y.; Limphirat, W.; Donphai, W.; Dittanet, P.; Chareonpanich, M.; Limtrakul, J. CO₂ hydrogenation to methanol over CuO-ZnO-ZrO₂-SiO₂ catalysts: Effects of SiO₂ contents. *Chem. Eng. J.* **2017**, *316*, 692–703. [[CrossRef](#)]
60. Wang, L.; Guan, E.; Wang, Y.; Wang, L.; Gong, Z.; Cui, Y.; Meng, X.; Gates, B.C.; Xiao, F.-S. Silica accelerates the selective hydrogenation of CO₂ to methanol on cobalt catalysts. *Nat. Commun.* **2020**, *11*, 1033. [[CrossRef](#)]
61. Liu, T.; Xu, D.; Wu, D.; Liu, G.; Hong, X. Spinel ZnFe₂O₄ Regulates Copper Sites for CO₂ Hydrogenation to Methanol. *ACS Sustain. Chem. Eng.* **2021**, *9*, 4033–4041. [[CrossRef](#)]
62. Singh, R.; Tripathi, K.; Pant, K.K. Investigating the role of oxygen vacancies and basic site density in tuning methanol selectivity over Cu/CeO₂ catalyst during CO₂ hydrogenation. *Fuel* **2021**, *303*, 121289. [[CrossRef](#)]
63. Rui, N.; Wang, Z.; Sun, K.; Ye, J.; Ge, Q.; Liu, C.-j. CO₂ hydrogenation to methanol over Pd/In₂O₃: Effects of Pd and oxygen vacancy. *Appl. Catal. B Environ.* **2017**, *218*, 488–497. [[CrossRef](#)]
64. Wu, P.P.; Yang, B. Significance of Surface Formate Coverage on the Reaction Kinetics of Methanol Synthesis from CO₂ Hydrogenation over Cu. *ACS Catal.* **2017**, *7*, 7187–7195. [[CrossRef](#)]
65. Kattel, S.; Ramirez, P.J.; Chen, J.G.; Rodriguez, J.A.; Liu, P. Active sites for CO₂ hydrogenation to methanol on Cu/ZnO catalysts. *Science* **2017**, *355*, 1296–1299. [[CrossRef](#)] [[PubMed](#)]
66. Carey, J.J.; Nolan, M. Enhancing the oxygen vacancy formation and migration in bulk chromium(III) oxide by alkali metal doping: A change from isotropic to anisotropic oxygen diffusion. *J. Mater. Chem. A* **2017**, *5*, 15613–15630. [[CrossRef](#)]
67. Chen, S.; Zhang, J.; Song, F.; Zhang, Q.; Yang, G.; Zhang, M.; Wang, X.; Xie, H.; Tan, Y. Induced high selectivity methanol formation during CO₂ hydrogenation over a CuBr₂-modified CuZnZr catalyst. *J. Catal.* **2020**, *389*, 47–59. [[CrossRef](#)]
68. Xu, D.; Hong, X.; Liu, G. Highly dispersed metal doping to ZnZr oxide catalyst for CO₂ hydrogenation to methanol: Insight into hydrogen spillover. *J. Catal.* **2021**, *393*, 207–214. [[CrossRef](#)]
69. Mureddu, M.; Lai, S.; Atzori, L.; Rombi, E.; Ferrara, F.; Pettinau, A.; Cutrufello, M.G. Ex-LDH-Based Catalysts for CO₂ Conversion to Methanol and Dimethyl Ether. *Catalysts* **2021**, *11*, 615. [[CrossRef](#)]
70. Martin, O.; Martín, A.J.; Mondelli, C.; Mitchell, S.; Segawa, T.F.; Hauert, R.; Drouilly, C.; Curulla-Ferré, D.; Pérez-Ramírez, J. Indium Oxide as a Superior Catalyst for Methanol Synthesis by CO₂ Hydrogenation. *Angew. Chem. Int. Ed.* **2016**, *55*, 6261–6265. [[CrossRef](#)]
71. Yao, L.; Pan, Y.; Wu, D.; Li, J.; Xie, R.; Peng, Z. Approaching full-range selectivity control in CO₂ hydrogenation to methanol and carbon monoxide with catalyst composition regulation. *Inorg. Chem. Front.* **2021**, *8*, 2433–2441. [[CrossRef](#)]
72. Fang, T.; Liu, B.; Lian, Y.; Zhang, Z. Selective Methanol Synthesis from CO₂ Hydrogenation over an In₂O₃/Co/C-N Catalyst. *Ind. Eng. Chem. Res.* **2020**, *59*, 19162–19167. [[CrossRef](#)]
73. Ahmad, K.; Upadhyayula, S. Kinetics of CO₂ hydrogenation to methanol over silica supported intermetallic Ga₃Ni₅ catalyst in a continuous differential fixed bed reactor. *Int. J. Hydrogen Energy* **2020**, *45*, 1140–1150. [[CrossRef](#)]
74. Temvuttirojn, C.; Poo-arporn, Y.; Chanlek, N.; Cheng, C.K.; Chong, C.C.; Limtrakul, J.; Witoon, T. Role of Calcination Temperatures of ZrO₂ Support on Methanol Synthesis from CO₂ Hydrogenation at High Reaction Temperatures over ZnOx/ZrO₂ Catalysts. *Ind. Eng. Chem. Res.* **2020**, *59*, 5525–5535. [[CrossRef](#)]

75. Kuwahara, Y; Mihogi, T; Hamahara, K; Kusu, K; Kobayashi, H; Yamashita, H. A quasi-stable molybdenum sub-oxide with abundant oxygen vacancies that promotes CO₂ hydrogenation to methanol. *Chem. Sci.* **2021**, *12*, 9902–9915. [[CrossRef](#)] [[PubMed](#)]
76. Kuchkina, N.V; Zinatullina, M.S; Serkova, E.S; Vlasov, P.S; Peregudov, A.S; Shifrina, Z.B. Hyperbranched pyridylphenylene polymers based on the first-generation dendrimer as a multifunctional monomer. *RSC Adv.* **2015**, *5*, 99510–99516. [[CrossRef](#)]

Disclaimer/Publisher's Note: The statements, opinions and data contained in all publications are solely those of the individual author(s) and contributor(s) and not of MDPI and/or the editor(s). MDPI and/or the editor(s) disclaim responsibility for any injury to people or property resulting from any ideas, methods, instructions or products referred to in the content.